Radiometric Correction of Landsat 8 Imagery Using Open-Source Software and its Impact on Spectral Index Derivation: A Case Study in the Southern Expanded Metropolitan Microregion of Espírito Santo State, Brazil

Wimerson S. Bazan [1, 3], Fernanda S. Y. Watanabe [2], Maria L. B. T. Galo [2], Antonio M. G. Tommaselli [2], Mauricio Galo [2]

[1] São Paulo State University - UNESP, Graduate Program in Cartographic Sciences,
Presidente Prudente, São Paulo, Brazil – wimerson.bazan@unesp.br
[2] São Paulo State University - UNESP, Dept. of Cartography,
Presidente Prudente, São Paulo, Brazil – fernanda.watanabe@unesp.br, trindade.galo@unesp.br, a.tommaselli@unesp.br, mauricio.galo@unesp.br
[3] Federal Institute of Espírito Santo - IFES, Coord. of Geomatics,
Vitória, Espírito Santo, Brazil – wimerson.bazan@ifes.edu.br

Keywords: Atmospheric Correction, i.atcorr, 6S Algorithm, Surface Reflectance, Radiometric Correction, Landsat 8.

Abstract

Orbital imagery acquired in the optical spectrum is inherently subject to geometric and radiometric errors. These inaccuracies stem from instrumental imperfections, imaging limitations, and various effects that influence the signal from the information source (targets) to the sensor. Most of these errors can be mitigated through radiometric calibration followed by atmospheric correction. Rigorous atmospheric correction requires data that allow for the estimation of scattering and absorption by atmospheric constituents at different wavelengths. Considering this context and aiming to enable the effective use of Landsat 8 satellite imagery (Level 1 processing) for spectral index-based change assessment, this study proposes a method based on radiometric data calibration followed by atmospheric correction using the 6S radiative transfer model, as implemented in the *i.atcorr* tool of the Geographic Resources Analysis Support System (GRASS GIS). Results, evaluated qualitatively and quantitatively, indicate that atmospheric correction using *i.atcorr* provides reliable outcomes only for the visible-red, near infrared, and shortwave infrared bands when assessing changes between two distinct epochs. For applications requiring the use of bands at the shortest wavelengths (blue and visible-green), which are more susceptible to atmospheric scattering effects, it is recommended to use Level 2 corrected images, processed by the LaSRC algorithm and provided by the U.S. Geological Survey (USGS).

1. Introduction

The challenge of atmospheric correction in orbital imagery has been a subject of study for at least 58 years (Hall et al., 1991), leading to methods based on scene characteristics or, alternatively, on radiative transfer models (Novo, 2010). The latter requires comprehensive knowledge of atmospheric parameters, including vertical profiles of water vapour, aerosols, and gases (e.g., O_2, O_3, CO_2, trace gases). Such data are crucial for the accurate conversion of raw sensor data into Surface Reflectance (SR), which in turn is essential for calculating accurate spectral indices, thereby enabling reliable change assessment across distinct periods and reliable monitoring of the land surface.

Based on this context, this study proposes an alternative approach for the radiometric correction of imagery from the Operational Land Imager (OLI) sensor aboard the Landsat 8 satellite (L8), Level 1 processing (L1). This approach was developed in two stages and includes both qualitative and quantitative assessments of the results. It is grounded in radiometric calibration (Ihlen, 2019), followed by atmospheric correction using the Second Simulation of the Satellite Signal in the Solar Spectrum algorithm (6S) (Vermote et al., 1997). Although a more recent version, known as 6SV – which accounts for the polarisation of radiation (Kotchenova and Vermote, 2007) – is available, the standard 6S version was chosen, given its implementation in *i.atcorr*, the atmospheric correction module available in GRASS GIS (GRASS Development Team, 2024) software.

To validate this approach, a case study was conducted in the Southern Expanded Metropolitan Microregion of Espírito Santo State, Brazil. In the first stage, the correspondence among three reflectance versions for each of the seven spectral bands of the OLI sensor was evaluated across the entire scene: Top of Atmosphere Reflectance (**L1_ToA**), Surface Reflectance corrected by *i.atcorr* (**L1_SR**), and Level 2 processed Surface Reflectance (**L2_SR**), provided by the U.S. Geological Survey (USGS). In the second stage, the study area was limited to the Microregion and five spectral indices were calculated for each reflectance version: Normalised Difference Vegetation Index (NDVI) (Rouse et al., 1973), Normalised Difference Water Index (NDWI) (Gao et al., 1997), Modified Normalised Difference Water Index (MNDWI) (Xu, 2006), Normalized Normalised Difference Built-up Index (NDBI) (Zha et al., 2003), and Burn Ratio (NBR) (Key and Benson, 1999).

Absolute differences between these spectral indices in two epochs, 2016 and 2020, were calculated for each of the three versions and compared using visual and regression analyses. This comparison enabled indirect inference regarding the relevance of atmospheric correction applied via *i.atcorr* for spectral index calculation aimed at change assessment between distinct epochs.

2. Study Area, Data, and Methods

2.1 Study Area

In the first stage, the study area encompassed the entire southern portion of Espírito Santo State, covered by the L8 scene in path/row 216/074. The second stage was limited to the Southern Expanded Metropolitan Microregion, comprising the municipalities of Alfredo Chaves, Anchieta, Iconha, Itapemirim, Marataízes, and Piúma (Figure 1). This microregion exhibits diverse geographical and land cover characteristics. Furthermore, it was cloud-free in both 2016 and 2020.

This contribution has been peer-reviewed. The double-blind peer-review was conducted on the basis of the full paper.
https://doi.org/10.5194/isprs-annals-X-3-W4-2025-27-2026 | © Author(s) 2026. CC BY 4.0 License.

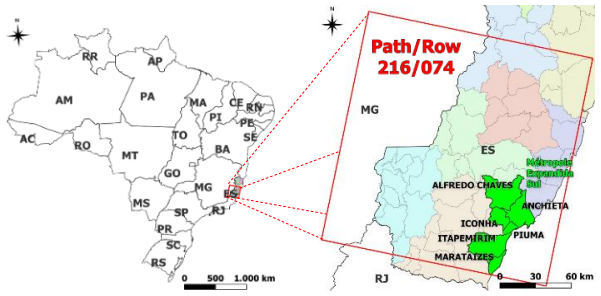

Figure 1. L8 Scene in Path/Row 216/074 and the Southern Expanded Metropolitan Microregion of Espírito Santo State.

2.2 Data

The data utilised comprise: seven spectral bands of the L8 OLI sensor (Table 1), Level 1 and Level 2 processing, acquired in path/row 216/074, on 16 June 2016 at 12:44:43 UTC and 27 June 2020 at 12:44:46 UTC; Aerosol Optical Depth (AOD) data; and SRTM Digital Elevation Model (DEM).

Sensor/ Spectrum	Band	Spectral Region	Wavelength (nm)	Resolutions
OLI/ Visible	B1	Coastal/ Aerosol	433 – 455	30 m (Spatial)
	B2	Blue	448 – 515	
	B3	Green	525 – 595	16 bits (Radiometric)
	B4	Red	633 – 677	
OLI/ Infrared	B5	NIR	845 – 855	
	B6	SWIR 1	1540 – 1672	16 days (Temporal)
	B7	SWIR 2	2073 – 2322	

Table 1. Spectral bands of the L8 OLI sensor. NIR refers to near-infrared and SWIR is shortwave infrared.

Level 2 data are generated using the LaSRC (Land Surface Reflectance Code) version 1.5.0. The original algorithm, developed by Dr. Eric Vermote and subsequently modified by the USGS, is detailed in Section 4.7 of the document describing the algorithm (USGS, 2025). The LaSRC code first generates the Top of Atmosphere (ToA) reflectance based on calibration parameters from the metadata and Equation 2 (Section 2.3). Subsequently, atmospheric correction routines are applied to the ToA reflectances, utilising auxiliary atmospheric data, such as water vapour and O_3, retrieved from the MODIS (Moderate Resolution Imaging Spectroradiometer) or VIIRS (Visible Infrared Imaging Radiometer Suite) sensors, and a 5-arcsecond DEM (ETOPO5). A separate routine is employed for aerosol retrieval in pixels identified as water.

AOD data measure the aerosol content along an atmospheric column. These data can be provided by ground-based stations from the AERONET (Aerosol Robotic Network) (Aeronet, 2024). However, the stations located in Brazil are few and distant from the study area. Another method of acquisition is through retrieval from orbital imagery, which can even be performed using L8 OLI images (Gayen et al., 2024), although this task proves to be largely impractical. Finally, a third alternative - which was adopted in this paper – utilises AOD values extracted from the MODIS collection, with a spatial resolution of 10 km.

These data are derived from collections by the MODIS sensor aboard the Terra (MOD04_L2) and Aqua (MYD04_L2) satellites. Regarding the algorithms used, the Dark Target (DT) exhibits high accuracy over dark regions, while the Deep Blue (DB) is recommended for high-reflectance areas, with a combined version also available (Elshora, 2023). Although data collected by MODIS aboard Terra have a smaller temporal lapse relative to the L8 acquisition, based on the coverage criterion, we opted for the AOD data collected via Aqua, which completely overlapped the L8 in path/row 216/074 in the 2016 (Figure 2a).

The AOD version adopted was the best estimate, based on the DB algorithm at wavelength of 550 nm. Conversely, in the 2020, the L8 scene was only partially covered considering this same AOD version (Figure 2b). Corrections by *i.atcorr* can be applied in two ways: 1) by using an atmospheric visibility map; or 2) by adopting a single AOD value at 550 nm. The visibility map can be obtained, by adapting Koschmieder's equation, through the substitution of the horizontal extinction coefficient with the AOD value (Wilson et al., 2015), leading to Equation 1:

$$V = 3.912 / AOD \quad (1)$$

where V is the atmospheric visibility in km. It should be noted that, according to Wilson et al. (2015), this substitution assumes that: 1) horizontal and vertical extinction coefficients are equal, 2) the relationship between horizontal visibility and the horizontal extinction coefficient is also valid for horizontal visibility and the vertical extinction coefficient, and 3) the vertical extinction profile has no effect on the AOD value. In 2016, visibility ranged between 50 km (darkest pixel) and 260 km (brightest pixel) (Figure 2c). For 2020, the range was between 40 and 260 km (Figure 2d). For the elevation data, a 30 m DEM obtained from SRTM was adopted (Figure 2e).

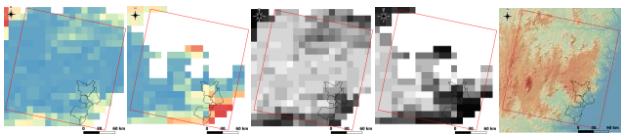

(a) (b) (c) (d) (e)

Figure 2. Data utilised by the 6S algorithm in *i.atcorr*: AOD at 550 nm for (a) 2016 and (b) 2020 epochs, visibility maps for (c) 2016 and (d) 2020, and (e) SRTM DEM.

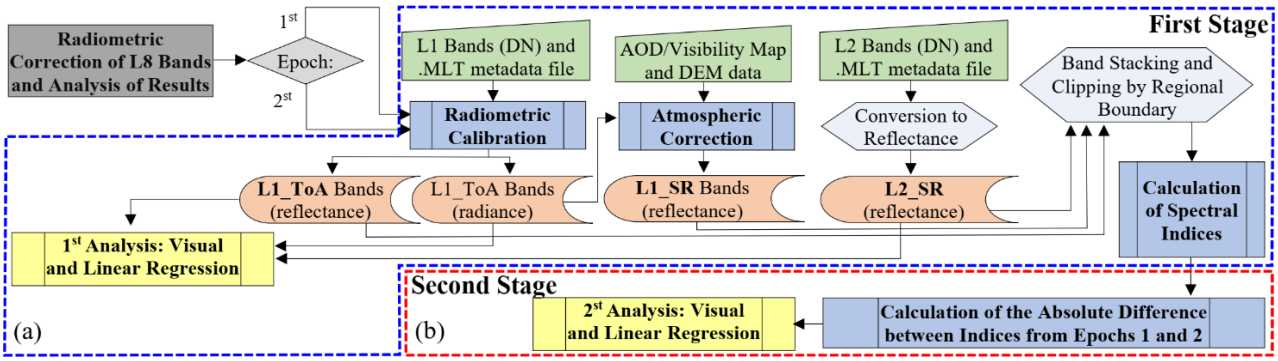

Figure 3. Flowchart of the proposed method, encompassing data processing and results analysis in two stages.

This contribution has been peer-reviewed. The double-blind peer-review was conducted on the basis of the full paper.
https://doi.org/10.5194/isprs-annals-X-3-W4-2025-27-2026 | © Author(s) 2026. CC BY 4.0 License.

2.3 Methods

The proposed method is presented by the flowchart in Figure 3, and comprises two stages, as described in the sequence. First stage (Figure 3a): Radiometric correction of all seven spectral bands (Table 1), undergoing radiometric calibration, followed by atmospheric correction by *i.atcorr*, and culminating in the initial qualitative (visual) and quantitative (regression) analyses. These analyses take into account the three spectral reflectance versions defined in Section 1: 1) L1_ToA; 2) L1_SR; and 3) L2_SR.

Regarding radiometric calibration, Ihlen (2019) mentions that images originally in 32 bits are processed in radiance units, and are converted to 16-bit integer Digital Numbers (DN) before being made available to the public as Level 1 data. However, these values can be converted to spectral reflectance or radiance using the additive and multiplicative factors provided by the ".MLT" metadata file, which is part of the Landsat 8 dataset. The Top of Atmosphere (ToA) reflectance for Level 1 processing (L1_ToA) can be obtained using Equation 2 (Ihlen, 2019).

$$\rho_\lambda = (M_\rho \times Q_{cal} + A_\rho)/sen(\theta_{SE}) \quad (2)$$

where ρ_λ is the Top of Atmosphere (ToA) spectral reflectance corrected for the solar elevation angle (θ_{SE}); M_ρ and A_ρ are the band-specific multiplicative and additive factors, respectively; and Q_{cal} represents the DN of the calibrated and quantised standard product.

However, to input into the 6S atmospheric correction algorithm implemented in *i.atcorr* – for further details on the 6S algorithm, refer to Vermote et al. (1997) – it is preferable that the data be in Top of Atmosphere (ToA) radiance (Watts/m².sr.µm), which can be obtained by using Equation 3. The result of the correction by *i.atcorr*, in turn, is saved as surface reflectance (L1_SR), scaled to the range of 0 to 1 (Ihlen, 2019):

$$L_\lambda = M_L \times Q_{cal} + A_L \quad (3)$$

where L_λ is the ToA radiance; M_L and A_L are the multiplicative and additive factors. Finally, the Level 2 data are converted to surface reflectance (L2_SR) by using Equation 4 (Sayle, 2024):

$$\rho_{\lambda s} = 2{,}75\times10^{-05} \times Q - 0{,}2 \quad (4)$$

where $\rho_{\lambda s}$ is the surface reflectance calculated from Q, which represents the DN of the Level 2 data. The values 2.75×10^{-05} and –0.2 are the multiplicative and additive factors, respectively. The first stage concludes with the spectral indices' computation: NDVI, NDWI, MNDWI, NBI, and NBR.

Second stage (Figure 3b): Calculation of absolute differences between the indices in the 2016 and 2020 years, within the micro-region boundaries (Figure 1), and evaluation of the results. Due to the existence of three reflectance versions to be intercompared, 15 absolute difference data were calculated for the five indices, with three for each specific index. As each index relates two bands from B3 to B7, the effectiveness of the atmospheric correction could indirectly be assessed through qualitative and quantitative analyses among the three versions of each spectral index.

3. Results and Discussion

3.1 Results and Discussion of the First Stage

The seven spectral bands were corrected by *i.atcorr* for both epochs, following the steps indicated in GRASS documentation (GRASS Development Team, 2024), with the tool accessed via QGIS software. The DEM (Figure 2e) was the sole data used in all processing, while the variables were: B1 to B7 in ToA radiance (Watts/m².sr.µm); configuration files; and visibility maps (Figures 2c and 2d) – or alternatively, mean AOD values at 550 nm.

The correction process for bands B1 to B7 was carried out sequentially, considering each epoch. The variables included (Figure 4): B1 to B7 in ToA radiance; configuration files in ".txt" format; and visibility maps (Figures 3c and 3d). The DEM (Figure 3e), as mentioned, remains constant throughout the correction process.

The adoption of visibility maps requires suppressing the line designated for AOD information in the ".txt" file, in addition to setting the visibility information to -1. Alternatively, if the visibility map is unavailable – which is more common – a single mean AOD value at 550 nm can be used, which must then be inserted into the .txt configuration file (GRASS Development Team, 2024).

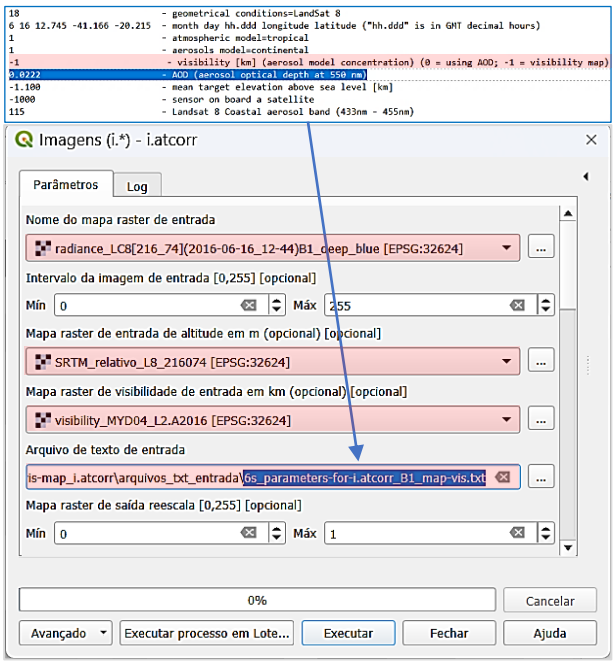

Figure 4. *i.atcorr* Configuration: input and pre-defined variables for atmospheric correction.

The configuration file, as well as the *i.atcorr* window, are illustrated in Figure 4. When using an AOD value, the entry for "visibility (km)" must be set to 0 (zero). In total, the file comprises up to 9 records containing the following information: 1) geometrical conditions code = 18 for Landsat 8; 2) month, day, hh.ddd, longitude and latitude ('hh.ddd' is in decimal hours GMT); 3) atmospheric model code = 1 for tropical regions; 4) aerosols model code = 1 for continental areas; 5) visibility [km] (aerosol model concentration), where code = 0 when intending to use AOD at 550 nm or code = -1 for using a raster visibility map (in which case, the next row must be suppressed); 6) AOD (aerosol optical depth at 550 nm); 7) mean target elevation above

This contribution has been peer-reviewed. The double-blind peer-review was conducted on the basis of the full paper.
https://doi.org/10.5194/isprs-annals-X-3-W4-2025-27-2026 | © Author(s) 2026. CC BY 4.0 License.

sea level [km] (here 1,100 m asl); 8) sensor on board a satellite; and 9) Landsat 8 band code, ranging from 115 to 123. For more details regarding the parameter configuration, see GRASS Development Team (2024).

Given the two possibilities, i.e., adopting the visibility maps (Figures 2c and 2d) or alternatively, mean AOD values at 550 nm, a preliminary experiment was conducted to evaluate the relevance of adopting a single AOD value instead of the visibility map. Bands B1 to B7 for 2016 year were corrected using the visibility map (Figure 2c), resulting in the L1_SR_VM data. Subsequently, these same bands underwent a new correction using a mean AOD value of 0.0222, calculated from Figure 2a data, yielding the L1_SR_AOD data.

The linear regression between these two corrected versions resulted in a slope (a) and intercept (b) close to 1 and 0, respectively, indicating a positive and strong correlation. The $R^2 = 1$ indicates that the linear model $y = ax \pm b$ explains 100% of the data's variability (Table 2).

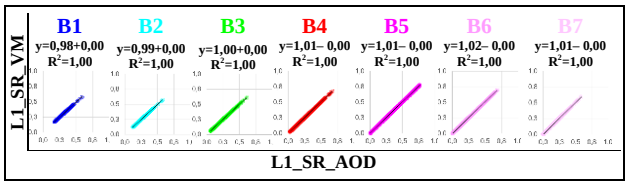

Table 2. Linear regression between the two versions of B1to B7, corrected by *i.atcorr* using the visibility map (L1_SR_VM), and a single AOD value (L1_SR_AOD).

Based on this analysis, the difference between the two corrected versions is disregarded. Henceforth, atmospheric correction for all bands utilised a single mean AOD value for both epochs, which proved to be convenient for this study, as the L8 scene collected at path/row = 216/074 on 27 June 2020 was not fully covered by AOD from the same day (Figure 2b). For 2020, a mean AOD value of 0.0308, obtained from Figure 3b data, was adopted.

In this subsection, qualitative and quantitative analyses were conducted, first for 2016 year (Tables 3 and 4), and then for 2020 (Tables 5 and 6). Tables 3 and 5 present the histograms of bands for each of the three reflectance versions: L1_ToA, L1_SR_AOD, and L2_SR, in 2016 and 2020, respectively. Meanwhile, Tables 4 and 6 provide the regression results between these same three versions. In the comparisons, L1_ToA data are taken as reference, while the L2_SR data are assumed more reliable, since the corrections were performed using the rigorous LaSRC code (Sayler, 2024).

Regarding the qualitative analysis of the 2016 data, by comparing the histograms in Table 3, it is evident that, compared to the L1_ToA version, the bands corrected by *i.atcorr* resulted in L1_SR_AOD with a subtle increase in brightness and a significant increase in contrast for B1 to B4. For B5, the brightness increase was slightly less pronounced, while B6 and B7 showed only contrast enhancements.

Furthermore, in comparison to L1_ToA, the L2_SR data present significant differences in brightness for bands from B1 to B5, which are severely affected by atmospheric absorption and scattering (Vermote et al., 1997), while the contrast remained nearly unchanged. Conversely, bands B6 and B7 showed no significant differences in brightness and contrast.

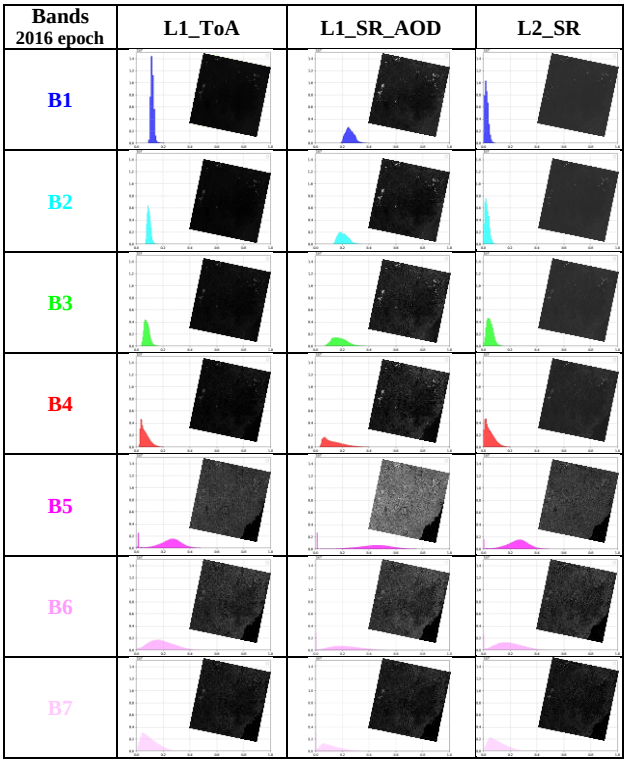

Table 3. Histograms of B1 to B7 for the reflectance versions in 2016: L1_ToA, L1_SR_AOD, and L2_SR.

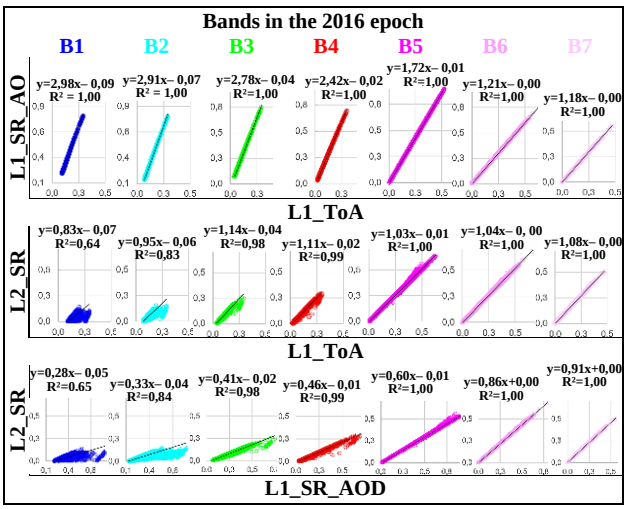

Table 4. Linear regressions between reflectances in 2016: L1_ToA, L1_SR_AOD, and L2_SR.

Regression analyses considering three combinations were employed in the quantitative analyses (Table 4). The first combination, which evaluates the variation of L1_SR_AOD relative to L1_ToA, yielded an $R^2 = 1$ for all bands. This indicates that the linear model $y = ax + b$ fully explains the variability between these data. The most significant differences in terms of contrast were observed for B1 to B4 (visible spectrum), where the range in slope was $2.42 \leq a \leq 2.98$. Conversely, for B5 to B7 (infrared spectrum), the range in slope was $1.18 \leq a \leq 1.72$, suggesting moderate contrasts. The intercept values (b) gradually decreased from B1 to B5, being zero for B6 and B7, indicating no increase in brightness for these bands.

The second combination, describing the variation of L2_SR relative to L1_ToA, resulted in coefficients of determination gradually increasing from B1 to B4, ranging from

$0.64 \leq R^2 \leq 0.99$, with $R^2 = 1$ for B5 to B7. This indicates that the linear model fully explains the variability between these data for the infrared bands. The slope ranged was $0.83 \leq a \leq 1.14$ for B1 to B4, and $1.03 \leq a \leq 1.08$ for B5 to B7, suggesting that the contrast remained nearly unchanged for the infrared bands. On the other hand, the intercept gradually decreased from B1 to B7, with values ranging from $0.02 \leq b \leq 0.07$ for B1 to B4 and $0.00 \leq b \leq 0.01$ for B5 to B7, implying practically no differences in brightness.

Finally, the third combination, presenting the variation of L2_SR relative to L1_SR_AOD, resulted in a coefficient of determination increasing from B1 to B4, ranging from $0.65 \leq R^2 \leq 0.99$, with $R^2 = 1$ for B5 to B7, indicating that the linear model fully explains the variability between the data for the infrared bands. The slope gradually increased from B1 to B7, ranging from $0.28 \leq a \leq 0.46$ for B1 to B4 and $0.60 \leq a \leq 0.91$ for B5 to B7, indicating a difference in contrast across all bands, with slightly smaller differences for the infrared ones. The intercept varied between $0.01 \leq b \leq 0.05$ for B1 to B4 and $0.00 \leq b \leq 0.01$ for B5 to B7, indicating a practically negligible difference in brightness for the infrared bands.

For the 2020 epoch, following the same steps, the qualitative analysis from Table 5 reinforces the observations made based on the 2016 data. Specifically, taking L1_ToA as a reference, the L1_SR_AOD data corrected by *i.atcorr* also showed increased brightness and contrast for B1 to B4 and only contrast for B5 to B7. Based on the same reference, L2_SR had a significant reduction in brightness for B1 to B4, and also for B5, maintaining practically the same histogram for B6 and B7.

Quantitative analyses from the charts in Table 6 address the same three previous combinations from Table 4, but this time related to the 2020 data. The results were very similar to those observed for the 2016 epoch. The first combination, which presents the variation of the *i.atcorr* corrected L1_SR_AOD relative to L1_ToA, resulted in an $R^2 = 1$ for all bands. The most significant differences in terms of contrast were observed for B1 to B4, with the slope ranging from $2.42 \leq a \leq 2.99$. The variation between $1.18 \leq a \leq 1.72$ for B5 to B7 confirms the modest contrasts for the infrared bands. The intercept gradually decreased from B1 to B7 and was zero for B6 and B7, implying no changes in brightness for these two bands.

The second combination, which presents the variation of L2_SR relative to L1_ToA, resulted in a coefficient of determination that gradually increased from B1 to B4, ranging from $0.64 \leq R^2 \leq 0.99$, with $R^2 = 1$ for B5 to B7. The slope varied between $0.47 \leq a \leq 1.08$ for B1 to B4 and $1.03 \leq a \leq 1.09$ for B5 to B7, meaning that the contrast remained practically the same for the infrared bands. The intercept also decreased from B1 to B7, ranging from $0.02 \leq b \leq 0.04$ for B1 to B4 and $0.00 \leq b \leq 0.01$ for B5 to B7, confirming the absence of significant changes in brightness.

The third combination, presenting the variation of L2_SR relative to the *i.atcorr*-corrected L1_SR_AOD, resulted in a gradual increase in the coefficient of determination from B1 to B4, ranging from $0.65 \leq R^2 \leq 0.99$, with $R^2 = 1$ for B5 to B7. The slope also gradually increased from B1 to B7, varying between $0.16 \leq a \leq 0.46$ for B1 to B4 and $0.60 \leq a \leq 0.92$ for B5 to B7, indicating that all bands showed differences in contrast, but slightly smaller for the infrared bands. The intercept varied between $0.01 \leq b \leq 0.02$ for B1 to B4 and $0.00 \leq b \leq 0.01$ for B5 to B7, again, pointing to an almost negligible brightness difference for the infrared bands.

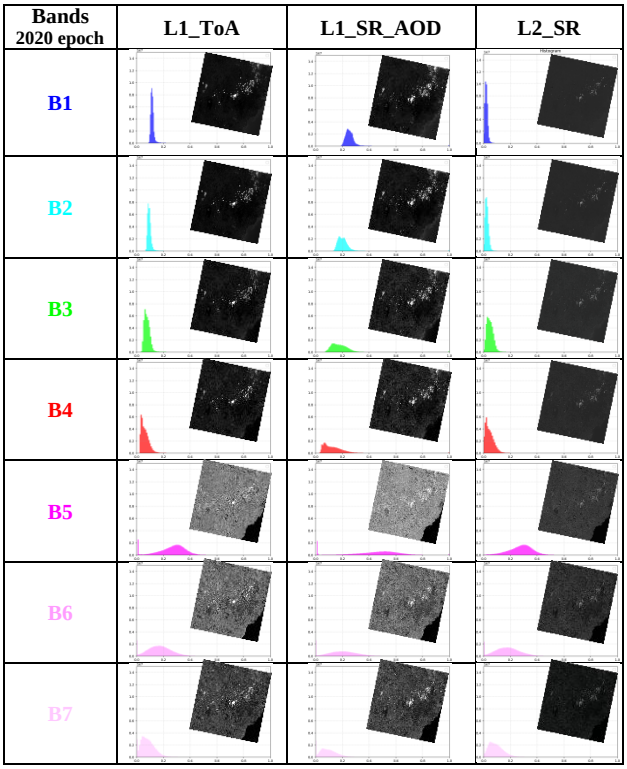

Table 5. Histograms of B1 to B7 for the reflectance versions in 2020: L1_ToA, L1_SR_AOD, and L2_SR.

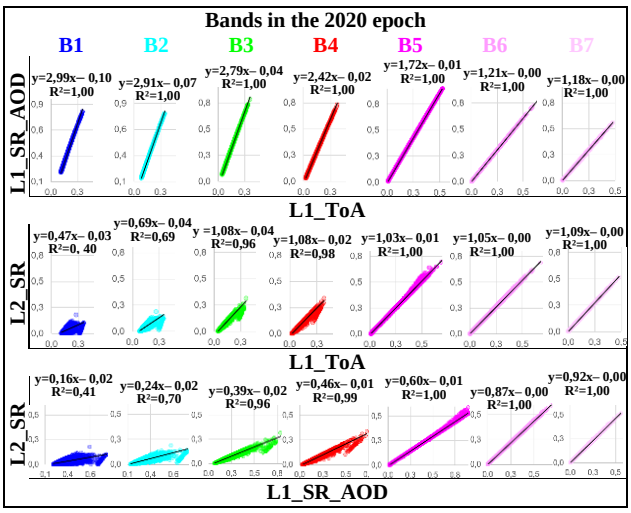

Table 6. Linear regressions between reflectances in 2020: L1_ToA, L1_SR_AOD, and L2_SR.

3.2 Results and Discussion of the Second Stage

The analysis in this section were based on five indices: NDVI, NDWI, MNDWI, NDBI, and NBR, calculated from reflectance versions L1_ToA, L1_SR_AOD, and L2_SR, and on the differences between these indices in both epochs, as outlined in the Figure 3. Tables 7 and 8 provide the indices for the 2016 and 2020 data, respectively, while Table 9 presents the absolute differences between these indices in both epochs, for each version of reflectance data. Additionally, the table provides the regression plots between these three versions of differences.

Finally, Table 10 presents the correlation matrix (Landim, 2004) calculated based on these absolute differences, enabling a complementary quantitative analysis.

Index 2016 epoch	Equation	B3 to B7 L1_ToA	B3 to B7 L1_SR_AOD	B3 to B7 L2_SR
NDVI	$\frac{B5-B4}{B5+B4}$			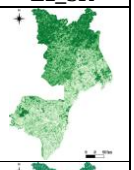
NDWI	$\frac{B5-B6}{B5+B6}$			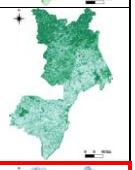
MNDWI	$\frac{B3-B6}{B3+B6}$		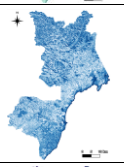	
NDBI	$\frac{B6-B5}{B6+B5}$	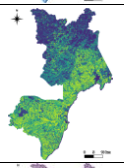		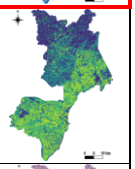
NBR	$\frac{B5-B7}{B5+B7}$			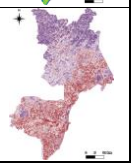

Table 7. Spectral indices: NDVI, NDWI, MNDWI, NDBI, and NBR based on reflectance data for the 2016 epoch.

Index 2020 epoch	Equation	B3 to B7 L1_ToA	B3 to B7 L1_SR_AOD	B3 to B7 L2_SR
NDVI	$\frac{B5-B4}{B5+B4}$			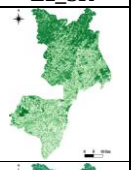
NDWI	$\frac{B5-B6}{B5+B6}$			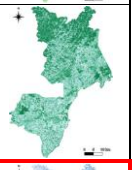
MNDWI	$\frac{B3-B6}{B3+B6}$			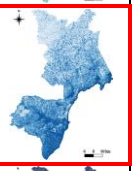
NDBI	$\frac{B6-B5}{B6+B5}$		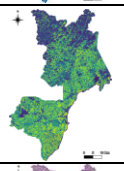	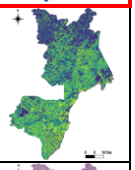
NBR	$\frac{B5-B7}{B5+B7}$			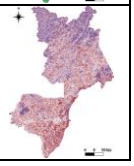

Table 8. Spectral indices: NDVI, NDWI, MNDWI, NDBI, and NBR based on reflectance data for the 2020 epoch.

Used Data	|Δ_NDVI|	|Δ_NDWI|	|Δ_MNDWI|	|Δ_NDBI|	|Δ_NBR|
B3 to B7 L1_ToA (1)		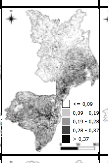	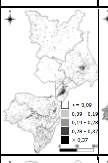	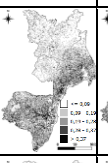	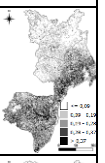
B3 to B7 L1_SR_ AOD (2)	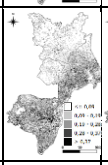	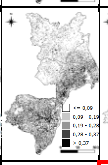	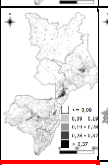	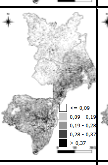	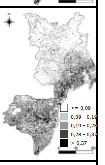
B3 to B7 L2_SR (3)	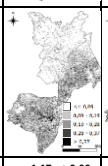	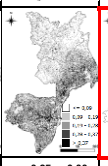	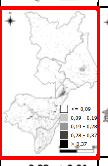	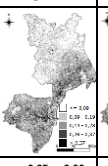	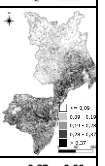
$\lvert\Delta_{indice}\rvert_{(1)}/\lvert\Delta_{indice}\rvert_{(2)}$	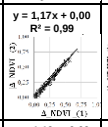	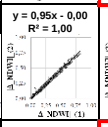	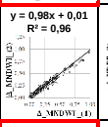	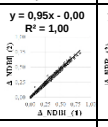	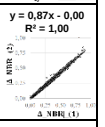
$\lvert\Delta_{indice}\rvert_{(1)}/\lvert\Delta_{indice}\rvert_{(3)}$	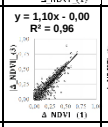	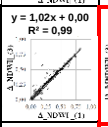	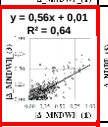	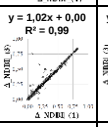	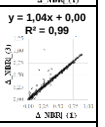
$\lvert\Delta_{indice}\rvert_{(2)}/\lvert\Delta_{indice}\rvert_{(3)}$	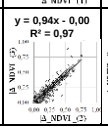	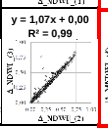	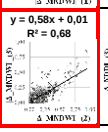	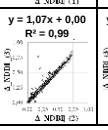	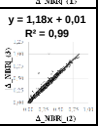

Table 9. Absolute differences between spectral indices in the 2020 and 2016 epochs, and regression plots between these differences for the three reflectance versions: L1_ToA, L1_SR_AOD, and L2_SR.

The first qualitative analysis was performed based on Tables 7 and 8. Each index, calculated for the three reflectance versions, allowed evaluating the effectiveness of the radiometric correction applied by *i.atcorr*, which produced the L1_SR_AOD version. Visually, all indices appeared similar to each other, except for the MNDWI, which exhibited considerable differences in the version calculated from L2_SR data (the most reliable one) in both epochs, when compared with the versions calculated from L1_ToA and L1_SR_AOD data. This can be attributed to the fact that visible bands are severely attenuated by the atmosphere, which affects the MNDWI calculated based on the green band B3.

The atmospheric correction of B3 by *i.atcorr*, as part of the L1_SR_AOD data version, failed to yield the spectral index MNDWI equivalent to that based on L2_SR. Instead, this index resembled the one derived from L1_ToA data (Tables 7 and 8). Although the NDVI is a function of the red band B4, no visual differences could be observed among this spectral index calculated for the three reflectance versions, leading to the finding that only B1 to B3 are affected by atmospheric attenuation. This is in accordance with the previous analysis based on Tables 4 and 6, whereas regressions of L1_ToA and L1_SR_AOD data relative to L2_SR resulted in the poorest correspondences, gradually decreasing from B3 to B1 in both epochs.

Table 9 presents the absolute differences between the five spectral indices in both the 2020 and 2016 epochs, for each reflectance version, complemented by regression plots. The qualitative analysis confirms the findings based on Tables 7 and

8, i.e., the two versions of absolute differences for the MNDWI index, calculated from L1_ToA and L1_SR_AOD data, were similar to each other, but significantly different from that obtained based on the L2_SR data. This reaffirms that the correction applied by *i.atcorr* to band B3 was ineffective.

The quantitative analysis supported by regressions, indicates that the correspondences among the absolute differences of the indices obtained from L1_ToA, L1_SR_AOD, and L2_SR showed: a coefficient of determination between $0.96 \leq R^2 \leq 1.00$; a slope between $0.87 \leq a \leq 1.18$; and an intercept between $0.00 \leq b \leq 0.01$, considering all spectral indices. These values suggest a high degree of similarity among these differences. The unique exception occurred with regressions involving the absolute differences of the MNDWI, specifically when the version obtained from L2_SR is correlated with the other two versions in the Table 9.

These findings are also corroborated by the correlation data highlighted in Table 10, where the absolute differences for the MNDWI index, calculated from L1_ToA and L1_SR_AOD data, showed correlations of 80% and 83%, respectively, with those obtained based on L2_SR data. It is also worth noting that the absolute differences among the three versions of the NDBI index showed a 100% correlation with the absolute differences calculated based on the three versions of the NDWI index, which is expected, given that the equations for calculating these two indices relate exactly the same bands, only with an inversion in the order of the bands B5 and B6 in the numerator (see equations in Tables 7 and 8).

		L1_ToA	L1_SR_AOD	L2_SR	L1_ToA	L1_SR_AOD	L2_SR	L1_ToA	L1_SR_AOD	L2_SR	L1_ToA	L1_SR_AOD	L2_SR	L1_ToA	L1_SR_AOD	L2_SR
		Δ_NDVI	Δ_NDVI	Δ_NDVI	Δ_NDWI	Δ_NDWI	Δ_NDWI	Δ_MNDWI	Δ_MNDWI	Δ_MNDWI	Δ_NDBI	Δ_NDBI	Δ_NDBI	Δ_NBR	Δ_NBR	Δ_NBR
L1_ToA	Δ_NDVI	1.00	1.00	0.98	0.85	0.86	0.86	0.39	0.40	0.32	0.85	0.86	0.86	0.89	0.89	0.89
L1_SR_AOD	Δ_NDVI		1.00	0.99	0.86	0.87	0.86	0.38	0.39	0.30	0.86	0.87	0.86	0.89	0.89	0.89
L2_SR	Δ_NDVI			1.00	0.85	0.86	0.85	0.38	0.39	0.30	0.85	0.86	0.85	0.89	0.89	0.89
L1_ToA	Δ_NDWI				1.00	1.00	1.00	0.58	0.60	0.41	1.00	1.00	1.00	0.97	0.96	0.97
L1_SR_AOD	Δ_NDWI					1.00	1.00	0.57	0.59	0.41	1.00	1.00	1.00	0.98	0.97	0.98
L2_SR	Δ_NDWI						1.00	0.57	0.59	0.41	1.00	1.00	1.00	0.96	0.96	0.97
L1_ToA	Δ_MNDWI							1.00	0.98	0.80	0.58	0.57	0.57	0.50	0.49	0.50
L1_SR_AOD	Δ_MNDWI								1.00	0.83	0.61	0.59	0.59	0.53	0.52	0.53
L2_SR	Δ_MNDWI									1.00	0.41	0.41	0.41	0.35	0.35	0.36
L1_ToA	Δ_NDBI										1.00	1.00	1.00	0.97	0.96	0.97
L1_SR_AOD	Δ_NDBI											1.00	1.00	0.98	0.97	0.98
L2_SR	Δ_NDBI												1.00	0.96	0.96	0.97
L1_ToA	Δ_NBR													1.00	1.00	1.00
L1_SR_AOD	Δ_NBR														1.00	1.00
L2_SR	Δ_NBR															1.00

Table 10. Correlation matrix between absolute differences calculated for three distinct versions for each of the spectral indices.

4. Considerations and Conclusions

Based on the analysis in Section 3, the *i.atcorr* atmospheric corrections for visible bands (B1 to B3) proved ineffective at fully compensating for atmospheric attenuation. This is clearly evidenced by the MNDWI, an index sensitive to B3: the MNDWI derived from L1_SR_AOD closely resembled that from the L1_ToA data, and both differed significantly from the more reliable L2_SR-based MNDWI. Although the *i.atcorr* correction did improve contrast slightly for bands B1 to B4 in the L1_SR_AOD product compared to L1_ToA, this partial improvement was insufficient to yield accurate surface reflectance in these crucial visible bands for spectral index calculations.

It is worth emphasising that the unique atmospheric data required by *i.atcorr*'s 6S algorithm is the AOD value (or the visibility map). Conversely, L2_SR data are corrected by the rigorous LaSRC code, which incorporates an adaptation of the 6S algorithm (Sayler, 2024) and considers the use of other atmospheric parameters, leading to more accurate corrections. For evaluating changes between distinct epochs, this study concludes that L8 OLI sensor data, corrected and evaluated by the proposed method, were suitable for calculating the spectral indices addressed herein, except for the MNDWI, for the reasons previously discussed.

In other words, the corrections were found to be satisfactory only for bands B4 to B7. Whether B2 and B3 need to be used in the calculation of any other indices, the use of the L2_SR data version is recommended. These conclusions align with Vermote et al. (1997)'s findings, which indicates that, due to the decoupling of absorption effects, the 6S algorithm is not recommended for correcting spectral bands with high atmospheric absorption. This is because the model fails to correctly simulate the interaction between high absorption and scattering, resulting in inaccurate results for visible bands, where aerosol interference is pronounced.

Acknowledgements

The authors would like to thank, for the PhD scholarship to the first author, the Coordenação de Aperfeiçoamento de Pessoal de Nível Superior (CAPES); the São Paulo Research Foundation (FAPESP) (grant number 21/06029-7); and the Pró-reitoria de Pós-graduação (PROPG) of Unesp for the 'Support for Faculty/ Student Participation in National and International Scientific Events' (Edital 32/2025-PROPG).

References

Aeronet. Aerosol Robotic Network. http://aeronet.gsfc.nasa.gov (11 December 2024).

Elshora, M., 2023. Evaluation of MODIS combined DT and DB AOD retrievals and their association with meteorological variables over Qena, Egypt. Environ Monit Assess, 195, 483. http://doi.org/10.1007/s10661-023-11118-8

Gao, B. C., 1997. NDWI normalized difference water index for remote sensing of vegetation liquid water from space. Remote Sensing of Environment, 58(3), 257-266.

Gayen, B.K., Acharya, P., Dutta, D., Sreekesh, S., 2024. Estimation of high-resolution aerosol optical depth (AOD) from Landsat and Sentinel images using SEMARA model over selected locations in South Asia. Atmospheric Research, 298, 107141. http://doi.org/10.1016/j.atmosres.2023.107141

GRASS Development Team. *i.atcorr* - GRASS GIS manual.

Open-Source Geospatial Foundation. https://grass.osgeo.org/grass-stable/manuals/i.atcorr.html (11 December 2024).

Hall, F.G., Strebel, D.E., Nickeson, J.E., Goetz, S.J., 1991. Radiometric rectification: Toward a common radiometric response among multidate, multisensor images. Remote Sensing of Environment, 35, 11–27. http://doi.org/10.1016/0034-4257(91)90062-B

Ihlen, V., 2019. Landsat 8 (L8) data users handbook. U.S Geological Survey. http://usgs.gov/core-science-systems/nli/landsat/landsat-8-data-users-handbook (11 December 2024).

Key, C. H., Benson, N. C.,1999. The Normalized Burn Ratio (NBR): A Landsat TM radiometric measure of burn severity. United States Geological Survey, Northern Rocky Mountain Science Center, Bozeman, MT, USA.

Kotchenova, S.Y., Vermote, E.F., 2007. Validation of a vector version of the 6S radiative transfer code for atmospheric correction of satellite data Part II Homogeneous Lambertian and anisotropic surfaces. Appl. Opt., 46, 4455. http://doi.org/10.1364/AO.46.004455

Landim, P.M.B., 2004: Análise estatística de dados geológicos. Unesp. Editora UNESP, São Paulo.

Liang, T., Liang, S., Zou, L., Sun, L., Li, B., Lin, H., He, T., Tian, F., 2022. Estimation of Aerosol Optical Depth at 30 m Resolution Using Landsat Imagery and Machine Learning. Remote Sensing, 14(5), 1053. http://doi.org/10.3390/rs14051053

Novo, E. M. L. M., 2010: Sensoriamento Remoto: princípios e aplicações. Editora Blucher, São Paulo.

Rouse, J. W., Haas, R. H., Schell, J. A., Deering, D. W.,1973. Monitoring vegetation systems in the Great Plains with ERTS. NASA Special Publication, 351(1), 309.

Sayler, K., 2024. Landsat 8-9 Collection 2 (C2) Level 2 Science Product (L2SP) Guide. U.S Geological Survey. http://usgs.gov/media/files/landsat-8-9-collection-2-level-2-science-product-guide (11 December 2024).

Vermote, E.F., Tanre, D., Deuze, J.L., Herman, M., Morcette, J.J., 1997. Second Simulation of the Satellite Signal in the Solar Spectrum, 6S: an overview. IEEE Trans. Geosci. Remote Sensing, 35, 675–686. http://doi.org/10.1109/36.581987

Wilson, R.T., Milton, E.J., Nield, J.M., 2015. Are visibility-derived AOT estimates suitable for parameterizing satellite data atmospheric correction algorithms? Int. J. Remote Sens. 36, 1675–1688. http://doi.org/10.1080/01431161.2015.1023558

Xu, H., 2006. Modification of normalised difference water index (NDWI) to enhance open water features in remotely sensed imagery. International Journal of Remote Sensing, 27(14), 3025-3033.

Zha, Y., Gao, J., & Ni, S., 2003. Use of normalized difference built-up index in automatically mapping urban areas from TM imagery. International Journal of Remote Sensing, 24(3), 583-594.

USGS, Landsat. Landsat 8–9 Calibration and Validation (Cal/Val) Algorithm Description Document (ADD); United States Geological Society: Sioux Falls, SD, USA, 2025. https://www.usgs.gov/media/files/landsat-8-9-calibration-validation-algorithm-description-document